

# Platinum Nanoparticles Generated in Functionality-Enhanced Reaction Media Based on Polyoctadecylsiloxane with Long-Chain Functional Modifiers

Eleonora V. Shtykova,<sup>†</sup> Dmitri I. Svergun,<sup>\*,†,‡</sup> Dmitri M. Chernyshov,<sup>§</sup> Irina A. Khotina,<sup>§</sup> Peter M. Valetsky,<sup>§</sup> Richard J. Spontak,<sup>||</sup> and Lyudmila M. Bronstein<sup>\*,§,⊥</sup>

*Institute of Crystallography, Russian Academy of Sciences, Leninsky pr. 59, 117333 Moscow, Russia, EMBL, Hamburg Outstation, Notkestrasse 85, D-22603 Hamburg, Germany, Nesmeyanov Institute of Organoelement Compounds, Russian Academy of Sciences, Vavilov St. 28, Moscow 117813, Russia, Departments of Chemical Engineering and Materials Science & Engineering, North Carolina State University, Raleigh, North Carolina 27695, and Department of Chemistry, Indiana University, Bloomington, Indiana 47405*

*Received: February 13, 2004; In Final Form: March 10, 2004*

Functionality-enhanced nanostructured matrices generated by intercalating polyoctadecylsiloxane (PODS) with octadecene (ODC) or octadecylamine (ODA) are employed as reaction media in which to grow Pt nanoparticles. Small-angle X-ray scattering (SAXS) signatures confirm that the amphiphilic PODS matrix orders into lamellae with a periodicity ( $d$ ) of 5.24 nm, which corresponds to the siloxy bilayer and a double layer of alkyl tails. The regular packing of the hydrophobic tails becomes distorted upon introduction of ODC or ODA. Incorporation of  $K[(C_2H_4)PtCl_3] \cdot H_2O$  (a Zeise salt) into the PODS/ODC matrix, followed by reduction of the Pt ions by  $NaBH_4$  or  $H_2$ , results in the localization of Pt compounds and nanoparticles along the siloxy bilayers, which remain dimensionally unchanged. Electron density profiles deduced from PODS/ODA, however, provide evidence for considerable structural reorganization upon metalation with  $H_2PtCl_6 \cdot 6H_2O$ . In this case, the siloxy bilayers broaden due to the presence of  $PtCl_6^{2-}$  ions, and the hydrophobic layers become distorted due to the formation of  $(PtCl_6^{2-})(ODAH^+)_2$  complexes. Subsequent reduction by  $NaBH_4$  restores the inherent PODS organization, while  $H_2$  reduction partially preserves the distorted matrix, indicating that some Pt nanoparticles form in close proximity to the siloxy bilayer. Transmission electron microscopy reveals that relatively monodisperse Pt nanoparticles measuring  $\sim 1$  nm in diameter are located along the siloxy bilayers, whereas anomalous SAXS further indicates that nanoparticles form aggregates of comparable size to  $d$  within the PODS double layers.

## Introduction

Organic macromolecules are widely used as matrices for the controlled formation of inorganic nanoparticles.<sup>1–17</sup> Once grown and stabilized within a polymer medium, metal nanoparticles typically retain their beneficial (e.g., catalytic or magnetic) properties while synergistically imparting new properties to the polymer. These hybrid organic/inorganic systems can therefore be far more robust for practical applications than, for instance, surfactant-stabilized nanoparticles. If the polymeric matrix inherently possesses nanostructural elements prior to the incorporation of metal precursors and subsequent nanoparticle formation, customized modulation of the nanoparticle spatial distribution within the polymer is possible. In fact, the presence of nanostructural features can be used to restrict the location and diffusion of metal-containing species, thereby providing subtle control over nanoparticle growth kinetics, particle size distribution, and particle positioning.<sup>9,17</sup> Characteristics such as these effectively govern the properties of hybrid nanomaterials and their potential use in emergent technologies. Narrow particle

size distribution, for instance, is a crucial consideration in the development of hybrid materials for applications requiring well-defined optical, magnetic, sensing, and catalytic properties. If candidate nanostructured polymers are soluble (as are most block copolymers,<sup>5,18,19</sup> dendrimers,<sup>10,20,21</sup> and polymer colloids<sup>9,22–24</sup>), their hybrid analogues will commonly exhibit comparable solubility, which ensures viable routes by which such materials can be (i) processed as films, coatings, or fibers or (ii) delivered to a designated location. In the case of nonsolvated nanostructured polymers such as ordered block copolymers in the bulk<sup>2,8,25</sup> or in thin films,<sup>15,26,27</sup> nanoparticles are normally grown, and consequently reside, in well-defined mesoscopic spatial regions, leading to improved control over nanoparticle growth and ultimate support.

Most polymeric materials of current interest in the production of precise metallic nanoparticles possess functional groups that can be used to control polymer metalation, as well as nanoparticle formation via adsorption of these groups on the nanoparticle surface.<sup>7,28,29</sup> This strategy can be readily applied to ordered block copolymers so that metal precursors complex, and nanoparticles form, exclusively with a specific chemical moiety in the copolymer, and nanoparticle position within the copolymer can be controllably manipulated.<sup>2,30</sup> In the absence of such functional groups, polymeric media can be loaded with metal compounds and nanoparticle growth can likewise be directed through size-regulated diffusion restrictions imposed, for instance, by the existence of nanoscale pores.<sup>12,13</sup> As we have

\* Corresponding authors. E-mail: Svergun@EMBL-Hamburg.de; lybronst@indiana.edu

<sup>†</sup> Institute of Crystallography, Russian Academy of Sciences.

<sup>‡</sup> EMBL.

<sup>§</sup> Nesmeyanov Institute of Organoelement Compounds, Russian Academy of Sciences.

<sup>||</sup> North Carolina State University.

<sup>⊥</sup> Indiana University.

TABLE 1: Elemental Composition of PODS and Hybrid PODS/FM Samples before and after Metalation

sample notations and chemical formulas	elemental analysis data, %									
	calculated					found				
	C	H	Si	N	Pt	C	H	Si	N	Pt
PODS, (C <sub>20</sub> H <sub>40</sub> SiO <sub>2</sub> )	70.6	11.8	8.2			69.9	11.2	8.4		
PODS/ODC, (C <sub>20</sub> H <sub>40</sub> SiO <sub>2</sub> ) <sub>4</sub> (C <sub>18</sub> H <sub>36</sub> )	73.0	12.2	7.0			72.7	12.5	6.6		
PODS/ODC–K[PtCl <sub>3</sub> (C <sub>2</sub> H <sub>4</sub> )]·H <sub>2</sub> O, (C <sub>20</sub> H <sub>40</sub> SiO <sub>2</sub> ) <sub>4</sub> (C <sub>18</sub> H <sub>36</sub> ) <sub>4</sub> {[PtCl <sub>3</sub> K]} <sub>x</sub> <sup>a</sup>	67.3	11.3	6.4		4.5	69.3	11.9	6.8		4.3
PODS/ODC–Pt–H <sub>2</sub> , (C <sub>20</sub> H <sub>40</sub> SiO <sub>2</sub> ) <sub>4</sub> (C <sub>18</sub> H <sub>36</sub> )Pt <sub>x</sub> <sup>a</sup>	69.6	11.6	6.6		4.6	70.1	12.2	6.7		4.4
PODS/ODC–Pt–NaBH <sub>4</sub> , (C <sub>20</sub> H <sub>40</sub> SiO <sub>2</sub> ) <sub>4</sub> (C <sub>18</sub> H <sub>36</sub> )Pt <sub>x</sub> <sup>a</sup>	69.6	11.6	6.6		4.6	69.0	12.0	6.8		4.2
PODS/ODA, (C <sub>20</sub> H <sub>40</sub> SiO <sub>2</sub> ) <sub>2</sub> (C <sub>18</sub> H <sub>41</sub> N)	73.2	12.7	5.9	1.5	–	74.1	13.0	6.1	1.4	
PODS/ODA–H <sub>2</sub> PtCl <sub>6</sub> ·6H <sub>2</sub> O, (C <sub>20</sub> H <sub>40</sub> SiO <sub>2</sub> ) <sub>2</sub> (C <sub>18</sub> H <sub>39</sub> N){[H <sub>2</sub> PtCl <sub>6</sub> ]0.5} <sub>x</sub> <sup>a</sup>	68.7	12.1	5.8	1.4	2.9	68.4	11.6	6.3	1.3	2.6
PODS/ODA–Pt–H <sub>2</sub> , (C <sub>20</sub> H <sub>40</sub> SiO <sub>2</sub> ) <sub>2</sub> (C <sub>18</sub> H <sub>39</sub> N)Pt <sub>0.5x</sub> <sup>a</sup>	71.0	12.3	5.7	1.4	3.0	71.3	12.2	6.5	1.4	2.5
PODS/ODA–Pt–NaBH <sub>4</sub> , (C <sub>20</sub> H <sub>40</sub> SiO <sub>2</sub> ) <sub>2</sub> (C <sub>18</sub> H <sub>39</sub> N)Pt <sub>0.5x</sub> <sup>a</sup>	71.0	12.3	5.7	1.4	3.0	70.4	11.9	6.1	1.3	2.4

<sup>a</sup>  $x$  is the complexation degree calculated from  $(100xyM_{\text{Pt}})/(\{z[\text{PODS}] + [\text{FM}]\}(1-x) + \{z[\text{PODS}] + [\text{FM}] + [\text{complex}]\}x) = f_{\text{Pt}}$ , where  $M_{\text{Pt}}$  is the atomic weight of Pt, [PODS] is the molecular weight of the PODS elementary unit, [FM] is the molecular weight of the corresponding modifier (ODC or ODA), {complex} is the molecular weight of the complex fragment attached to the corresponding hybrid siloxane matrix ({PtCl<sub>3</sub>K} for Zeise salt and {H<sub>2</sub>PtCl<sub>6</sub>/2} for platinic acid),  $z$  is the modification degree (4 for ODC and 2 for ODA),  $y$  is the metal/modifier ratio (1 for ODC and 0.5 for ODA),  $f_{\text{Pt}}$  is the metal content obtained from the elemental analysis. Calculated from this formula,  $x$  is equal to 0.4 for K[PtCl<sub>3</sub>(C<sub>2</sub>H<sub>4</sub>)] and 0.3 for H<sub>2</sub>PtCl<sub>6</sub>.

previously reported,<sup>16,17</sup> these two modes by which nanoparticle growth and position can be tailored within nanostructured polymer matrices can be combined through the use of polyoctadecylsiloxane (PODS), a self-organized polymer prepared by the hydrolytic condensation of octadecyltrichlorosilane and shown<sup>31</sup> to exhibit a layered nanostructure. Each siloxy bilayer of PODS consists of silanol groups separated by a molecularly thin water channel that provides excellent control over metal nanoparticle formation from dissolved organometallic salts. Our prior studies have established that the size of metal nanoparticles generated within the siloxy bilayers of PODS is virtually independent of metal species, metal concentration, and reducing agent. Unfortunately, the degree of metal incorporation achieved thus far is unacceptably low due to the relatively low inherent functionality of PODS. To overcome this material drawback, we propose that the functionality of PODS can be improved through intercalation with long-chain functional modifiers (FMs). These functionality-enhanced hybrids can then be loaded with metal compounds and serve as well-defined nanostructured media for nanoparticle formation, providing control over both particle size distribution and particle organization (positioning).

In the present work, we describe two intercalated PODS/FM systems as nanostructured media in which to grow designer Pt nanoparticles. Platinum has been chosen here to facilitate structural analysis by anomalous small-angle X-ray scattering (ASAXS), which has been successfully employed to (i) distinguish the scattering contributions from a metal and its surrounding environment, and (ii) monitor the formation of metal nanoparticles in a variety of polymer matrices.<sup>17,32–34</sup> In this emerging analytical technique, the dependence of atomic scattering on X-ray wavelength<sup>32,35,36</sup> augments the atomic contribution to scattering at energies near the atomic absorption edge. Together, ASAXS and transmission electron microscopy (TEM) permit detailed examination of the nanostructure of functionality-enhanced PODS, as well as Pt nanoparticle morphology and location within the polymer matrix.

## Experimental Section

**Materials.** Octadecyltrichlorosilane (OTS), *n*-octadecene (C<sub>18</sub>H<sub>36</sub>, abbreviated ODC), and *n*-octadecylamine (C<sub>18</sub>H<sub>37</sub>NH<sub>2</sub>, abbreviated ODA) were all purchased from Fluka (Switzerland) and used without further purification. All solvents were reagent-grade quality from Aldrich (Milwaukee, WI) and were used after distillation. The NaBH<sub>4</sub> reducing agent (Riedel-de-Haën, Ger-

many), H<sub>2</sub>PtCl<sub>6</sub>·6H<sub>2</sub>O salt (Reakhim, Russia), and K[(C<sub>2</sub>H<sub>4</sub>)PtCl<sub>3</sub>]·H<sub>2</sub>O salt (Aldrich) were used as-received, as was the H<sub>2</sub> gas (Reakhim). Water was purified with a Milli-Q water purification system.

**Synthesis.** The PODS was synthesized according to the method described elsewhere.<sup>31</sup> Addition of the functional modifiers (ODC and ODA) to the PODS matrix was achieved by direct intercalation of ODC (PODS/ODC) or ODA (PODS/ODA) into a suspension of pristine PODS within alcohol (20 g/L) containing a predetermined amount of a modifier (the molar ratios of C=Si and NH<sub>2</sub>/Si were maintained at 1:1). The suspension was stirred for 24 h at ambient temperature, isolated by filtration, washed with a copious amount of 50/50 w/w water/ethanol mixture, and dried in a vacuum desiccator overnight. The Pt precursor salts, K[(C<sub>2</sub>H<sub>4</sub>)PtCl<sub>3</sub>]·H<sub>2</sub>O and H<sub>2</sub>PtCl<sub>6</sub>·6H<sub>2</sub>O, were added to the ethanol suspensions containing PODS/ODC and PODS/ODA, respectively, in amounts corresponding to a molar Si/Pt ratio of 1:1. After 24 h of agitation at ambient temperature, the Pt-containing polymers were isolated, washed with ethanol, and dried in a vacuum desiccator overnight. Reduction of the Pt-filled PODS/ODC and PODS/ODA suspensions in a 50/50 w/w water/acetone mixture was conducted using either NaBH<sub>4</sub> (5-fold molar excess) or H<sub>2</sub> bubbled through the reaction solution for 30 min. After reduction of the Pt ions to metallic Pt, the polymer suspensions were stirred for 24 h, isolated, washed with excess ethanol, and dried overnight under vacuum. Elemental compositions of the ODC/ODA-modified and metalated PODS samples investigated in this work are summarized in Table 1.

**Methods. Transmission Electron Microscopy.** Electron-transparent specimens for transmission electron microscopy (TEM) were prepared by sectioning epoxy-embedded samples on a Leica Ultracut-S ultramicrotome. Images of the unstained specimens were acquired digitally with a CCD camera mounted on a LEO EM912 electron spectroscopic microscope operated at an accelerating voltage of 120 kV and an energy-filter ( $\Delta E$ ) setting of 0 eV. Digital images were analyzed with the Digitalmicrograph software package and enhanced for presentation with the Photoshop software suite.

**Small-Angle X-ray Scattering.** The ASAXS measurements were performed at the beamline JUSIFA<sup>37</sup> on the storage ring DORIS III of the Deutsches Elektronen Synchrotron (DESY, Hamburg) at four photon energies ( $E$ ) near the  $L_3$  absorption edge of Pt ( $E = 11.482, 11.530, 11.550, \text{ and } 11.559 \text{ keV}$ ). The

atomic scattering factor can be written as

$$f(E) = f_0 + f'(E) + if''(E) \quad (1)$$

where  $f'(E)$  and  $f''(E)$  are the anomalous dispersion corrections, which become considerable in the vicinity of the edge. The scattering intensity ( $I$ ) was recorded as a function of momentum transfer ( $s$ ) given by  $4\pi \sin\theta/\lambda$ , where  $2\theta$  is the scattering angle and  $\lambda$  is the wavelength (with  $\lambda$  [nm] =  $1.24/E$  [keV]). The differences between the scattering curves recorded at different photon energies near the  $L_3$  edge were proportional to the scattering from Pt atoms. These differences were consequently used to compute the particle size distribution functions by the indirect transform program GNOM<sup>38</sup> with the assumption that the particles were spherical. The program solved the integral equation

$$I(s) = (\Delta\rho)^2 \int_{R_{\min}}^{R_{\max}} D_V(R) m(R) i_0(sR) dR \quad (2)$$

where  $R$  is the radius of a sphere,  $R_{\min}$  and  $R_{\max}$  are the minimum and maximum radii, respectively,  $i_0(x) = \{[\sin(x) - x \cos(x)]/x^3\}^2$  and  $m(R) = (4\pi/3)R^3$ , are the sphere form factor and volume, respectively. The size distribution of the particles,  $N(R)$ , is represented here in terms of the volume distribution function as  $D_V(R) = m(R)N(R)$ . The scattering length density of anomalous atoms is given by  $\Delta\rho = (N_0^2 - N_k^2)e/v_{\text{at}}$ , where  $N$  and  $N_k$  are the populations of electrons contributing to scattering from the resonance at  $\lambda = \lambda_k$  ( $k = 1, 2, 3$ ),  $e$  is the Thompson electron radius, and  $v_{\text{at}}$  is the atomic volume. In computing  $D_V(R)$ , the value of  $R_{\min}$  was set equal to zero, whereas that of  $R_{\max}$  was selected for each individual data set by successive trials with different parameter values.

The internal structure of the polymer matrix was characterized using the program PEAK<sup>39</sup> by fitting Gaussian profiles to interactively selected Bragg peaks in the scattering patterns. The long-range order dimension ( $L$ ) and the degree of disorder in the system ( $\Delta/\bar{d}$ ) were determined from the following expressions:<sup>40</sup>

$$L = \frac{\lambda}{\beta_s \cos\theta} \quad (3)$$

$$\Delta/\bar{d} = \frac{1}{\pi} \sqrt{\frac{\beta_s \cdot \bar{d}}{\lambda}} \quad (4)$$

where  $\beta_s$  is the full width at half-maximum intensity of the peak (in radians) observed at a mean scattering angle of  $2\theta$ ,  $\bar{d} = 2\pi/s_{\max}$  is the characteristic size (periodicity or spacing) of the diffracting structure corresponding to the peak position  $s_{\max}$ , and  $\Delta$  is the mean-square deviation of the distance between neighboring layers.

A one-dimensional Fourier transformation was used to compute the centrosymmetric electron density profiles along the direction perpendicular to the plane of the PODS lamellae, viz.,

$$\rho(r) = \sum_{l=1}^N s_l A(s, l) = \sum_{l=1}^N s_l \sin \pi s r [\pm \sqrt{S(l)}] \quad (5)$$

where  $N$  is the number of peaks, and  $s_l$  and  $S(l)$  are the position and area of the  $l$ th Bragg peak, respectively. All combinations of signs of  $A(s, l)$  were considered and the most plausible was selected by visual inspection of the density profiles on the basis of the known chemical composition of PODS. The scattering

profiles were (low-pass) filtered over the period of the termination wave  $T = 2\pi/s_N$  to reduce the termination effect. The PODS powders were measured in 1 mm thick aluminum cuvettes (with mica windows) placed in a vacuum to diminish parasitic scattering. Two sample-to-detector distances, 935 and 3635 mm, were used to probe the ranges  $0.4 < s$  (nm<sup>-1</sup>)  $< 7.3$  and  $0.08 < s$  (nm<sup>-1</sup>)  $< 1.5$ , respectively. The scattering patterns, corrected for background scattering and fluorescence, were merged to cover the entire experimental scattering range of interest.

## Results and Discussion

**Composition of Modified Pt-Filled PODS.** Table 1 indicates that the incorporation of the functional modifiers (FMs) ODC and ODA into the pristine PODS depends on the type of the modifier. According to the tabulated elemental composition results, intercalation with ODC yields a mixed structure containing about one ODC molecule for every four PODS units. Incorporation of ODA is more efficient, as the functionality-enhanced hybrid contains one ODA molecule for approximately every two PODS units. When ODA or ODC molecules are inserted into the PODS lamellar structure, the polymer matrix becomes more highly functionalized so that metal precursors can be assigned to the location of the newly introduced functional groups. To ensure interaction with the ODC double bond, a Zeise salt, which readily exchanges ethylene for various olefins,<sup>41,42</sup> has been selected. In the case of ODA with its amino group, we have elected to choose platinic acid, H<sub>2</sub>PtCl<sub>6</sub>, as the precursor to metallic Pt, since it promotes protonation of the ODA amino group, thus providing a strong electrostatic interaction between the two monovalent ODAH<sup>+</sup> cations and the divalent PtCl<sub>6</sub><sup>2-</sup> anion.<sup>42</sup>

### Structural Characteristics of Modified Pt-Filled PODS.

**Internal structure of modified PODS.** To elucidate changes in the structure of the functionalized PODS systems during metalation (i.e., incorporation of Pt precursors and Pt nanoparticle formation), one must first consider the possible structural variations of PODS in the presence of the FMs intercalated here. Figure 1 is a series of SAXS patterns collected from PODS, as well as the PODS/ODC and PODS/ODA hybrid matrices. Visual comparison of these data does not reveal significant changes of the scattering patterns after introduction of the two FMs into the PODS lamellae. All scattering curves display pronounced Bragg reflections at integral spacing ratios ( $d$ ,  $d/2$ ,  $d/3$ , etc.) due to the lamellar nanostructure. Structural parameters extracted from the SAXS patterns displayed in Figure 1 are listed in Table 2. Recall that the mean long-range order dimension ( $L$ ) estimates the size of the quasi-crystalline zones in the samples, whereas the degree of disorder ( $\Delta/\bar{d}$ ) provides the relative mean square deviation of the distance between neighboring periodic motifs. These structural metrics computed from the first Bragg peak in each SAXS pattern coincide with each other (within experimental error) for the unmodified and hybrid PODS matrices, which exhibit a relatively high degree of order. According to the data in Table 2,  $\Delta/\bar{d}$  is  $\sim 0.12$ . A system is considered poorly ordered at a  $\Delta/\bar{d}$  value of 0.15 (as a point of reference, the Bragg peaks nearly disappear when  $\Delta/\bar{d} > 0.25$ ).<sup>40</sup>

Moreover, the periodicity ( $d$ ) ascertained for all the samples is virtually identical within experimental error, in which case  $d = 5.24$  nm is used to generate the electron density profiles across the PODS bilayer from the integrated peak intensities presented in Figure 2. The sign combination in eq 5 is chosen by visual examination of the computed density profiles taking into account known the chemical constitution of PODS: a centrosymmetric density profile is expected to show a maximum in the middle



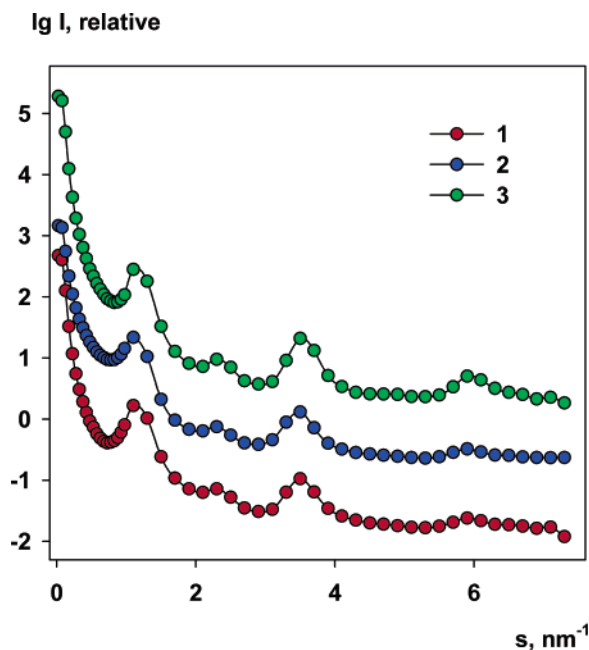


**Figure 1.** SAXS patterns acquired from pristine PODS (1), PODS/ODC (2), and PODS/ODA (3). In this and subsequent figures, successive datasets are shifted down by 1 order of magnitude to facilitate visualization, and the statistical error bars are smaller than the symbols used.

of the bilayer due to the high electron density of the Si atoms. Another feature of the profile is a pronounced interval of nearly constant electron density on both sides of the maximum corresponding to regularly packed alkyl tails. Last, the electron density in close proximity to the boundary of the PODS bilayer must decrease due to localized disordering at the tail–tail interface. Thus, the sign set  $[- + - - -]$  for  $l = 1, 2, 3, 5, 6$  has been used to compute the electron density profile on the presumption that six peaks are generally discernible on the experimental scattering patterns. The density reconstruction is conducted in relative units, since the position of the  $l = 0$  reflection is not available. It is important to recognize that, due to the relatively low resolution of this methodology ( $2\pi/s_{\text{max}} = 1$  nm), the double row of Si atoms in the PODS siloxy bilayer is not expected to be resolved, thereby yielding a single maximum in the density profile.

Interaction of pristine PODS with the two FMs employed here renders a visible increase in electron density in the middle of the alkyl tail region of PODS (cf. Figure 2). This distinguishing characteristic is more noticeable for PODS modified with ODC, despite the lower level of ODC incorporation relative to that of ODA, and can be explained on the basis of embedding the FM molecules between the hydrophobic tails of PODS. More specifically, a polar ODA amino group is expected to reside near the siloxy bilayer of PODS to minimize hydrophobic repulsion with the alkyl tails. In the event that the ODA amino groups form hydrogen bonds with silanol (Si–OH) groups, incorporation of ODA in PODS may become more favorable (as illustrated in Scheme 1), resulting in a slight increase in the hydrocarbon layer electron density. Unlike ODA, ODC is completely hydrophobic, in which case the position of the functional double bonds should be random (see Scheme 1). Since there is no driving force to position ODC near the siloxy bilayer, a lower electron density is observed in close proximity to the siloxy bilayer in Figure 2. Conversely, the electron density increases within the hydrocarbon layer due to the increased packing density of the PODS alkyl tails intercalated with ODC.

Note that functional modification of PODS via incorporation of either ODC or ODA does not change the structure of the siloxy double layer, as evidenced by the half-width of the central peak remaining constant at  $\sim 1$  nm for all PODS samples.

**Internal Structure of Modified Pt-Filled PODS/ODC.** Experimental scattering profiles acquired from different compositions of PODS/ODC measured at an incident-beam energy far from the absorption edge of Pt are presented in Figure 3 and confirm that the lamellar nanostructure of the PODS matrix is preserved in all cases. In this case, addition of a Zeise salt, as well as subsequent reduction of the metal ions with both  $\text{NaBH}_4$  and  $\text{H}_2$ , induces no significant change in scattering from that of pristine PODS. The structural parameters extracted from the scattering patterns displayed in Figure 3 are provided in Table 2 and are identical within experimental error. The values of the tabulated structural parameters have been calculated from the first Bragg reflections according to eqs 3 and 4. Some subtle differences in the scattering patterns are evident in the vicinity of the second- and fifth-order peaks (the fourth- and sixth-order peaks are absent). To establish a clear picture of the nanostructural changes that occur during metal particle formation in PODS/ODC, we have computed the electron density profiles from integral peak intensities according to the procedure described in the previous section. The resultant profiles, shown in Figure 4, indicate that neither functionalization of pristine PODS nor any further treatments (i.e., introduction or reduction of the Zeise salt) substantially changes the structure of the siloxy bilayer (the half-width of the central peak remains  $\sim 1$  nm in all samples). Alterations to the density profile are, for the most part, observed in the alkyl tail regions of the PODS/ODC system. Embedding the Zeise salt, followed by subsequent reduction of the Pt ions with  $\text{NaBH}_4$  or  $\text{H}_2$ , promotes a significant density increase in the region adjacent to the siloxy bilayer. This observation suggests that, after ODC/salt complexation, the newly formed complex repositions itself within the hydrophobic layer so that the polar group locates near the siloxy bilayer. Further nucleation is anticipated to occur in the same region. Since the Pt nanoparticles are located regularly, they do not induce system disordering, and the density profiles closely resemble that of pristine PODS.

**Internal Structure of Modified Pt-Filled PODS/ODA.** Figure 5 shows SAXS patterns obtained from PODS with and without ODA. Included for comparison are data acquired from PODS/ODA with the complex formed by  $\text{H}_2\text{PtCl}_6$  before and after Pt ion reduction in the presence of  $\text{NaBH}_4$  or  $\text{H}_2$ . Unlike the PODS/ODC system, addition of  $\text{H}_2\text{PtCl}_6$  significantly alters the scattering pattern. While the inherent PODS lamellar nanostructure and the lamellar spacing are preserved (see Table 2), the appearance of the fourth- and sixth-order peaks provides evidence for major structural reorganization, as analyzed below in terms of the electron density profile. Before delving into the density profiles, it is noteworthy that reduction of the Pt complexes with either  $\text{NaBH}_4$  or  $\text{H}_2$  almost completely restores the initial PODS/ODA bilayer ordering, which is likewise characteristic of the PODS/ODS system. The electron density profiles provided for PODS/ODA in Figure 6 exhibit pronounced structural reorganization upon metalation. The half-width of the central peak,  $\sim 1$  nm for PODS and PODS/ODA, increases to 1.6 nm for the PODS/ODA– $\text{H}_2\text{PtCl}_6$  complex. This increase signifies that the Si interatomic distance in the siloxy bilayer is enlarged. Profound changes in electron density are also observed in the vicinity of the alkyl tails of PODS. These differences between the PODS/ODA and PODS/ODC systems may be related to the structure of the Pt complex. When platinum

TABLE 2: Structural Characteristics of Pristine and Pt-Containing PODS

sample	$s_1$ (nm <sup>-1</sup> )	$L$ (nm)	$\Delta/\bar{d}$	$\bar{d}$ (nm)
PODS	$1.19 \pm 0.01$	$35.0 \pm 2.0$	$0.12 \pm 0.01$	$5.28 \pm 0.05$
PODS/ODC	$1.17 \pm 0.01$	$35.0 \pm 2.0$	$0.12 \pm 0.03$	$5.35 \pm 0.06$
PODS/ODC-K[PtCl <sub>3</sub> (C <sub>2</sub> H <sub>4</sub> )]·H <sub>2</sub> O	$1.18 \pm 0.01$	$40.0 \pm 2.0$	$0.11 \pm 0.02$	$5.33 \pm 0.06$
PODS/ODC-K[PtCl <sub>3</sub> (C <sub>2</sub> H <sub>4</sub> )]·H <sub>2</sub> O-NaBH <sub>4</sub>	$1.19 \pm 0.01$	$44.0 \pm 4.0$	$0.11 \pm 0.01$	$5.26 \pm 0.05$
PODS/ODC-K[PtCl <sub>3</sub> (C <sub>2</sub> H <sub>4</sub> )]·H <sub>2</sub> O-H <sub>2</sub>	$1.20 \pm 0.03$	$39.0 \pm 2.0$	$0.12 \pm 0.01$	$5.24 \pm 0.04$
PODS/ODA	$1.20 \pm 0.01$	$38.0 \pm 3.0$	$0.12 \pm 0.03$	$5.23 \pm 0.03$
PODSODA-H <sub>2</sub> PtCl <sub>6</sub> ·6H <sub>2</sub> O	$1.21 \pm 0.02$	$43.0 \pm 4.0$	$0.11 \pm 0.03$	$5.20 \pm 0.06$
PODS/ODA-H <sub>2</sub> PtCl <sub>6</sub> ·6H <sub>2</sub> O-NaBH <sub>4</sub>	$1.19 \pm 0.02$	$36.0 \pm 5.0$	$0.12 \pm 0.03$	$5.14 \pm 0.07$
PODS/ODA+H <sub>2</sub> PtCl <sub>6</sub> ·6H <sub>2</sub> O-H <sub>2</sub>	$1.20 \pm 0.02$	$30.0 \pm 5.0$	$0.13 \pm 0.03$	$5.18 \pm 0.05$

$\rho$ , relative

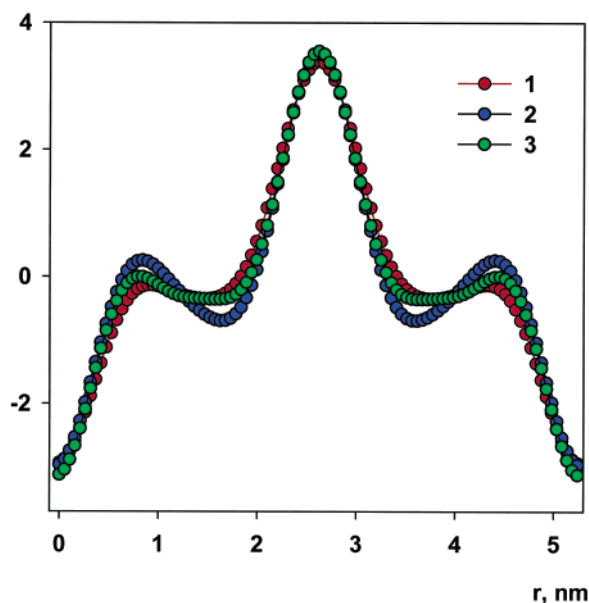
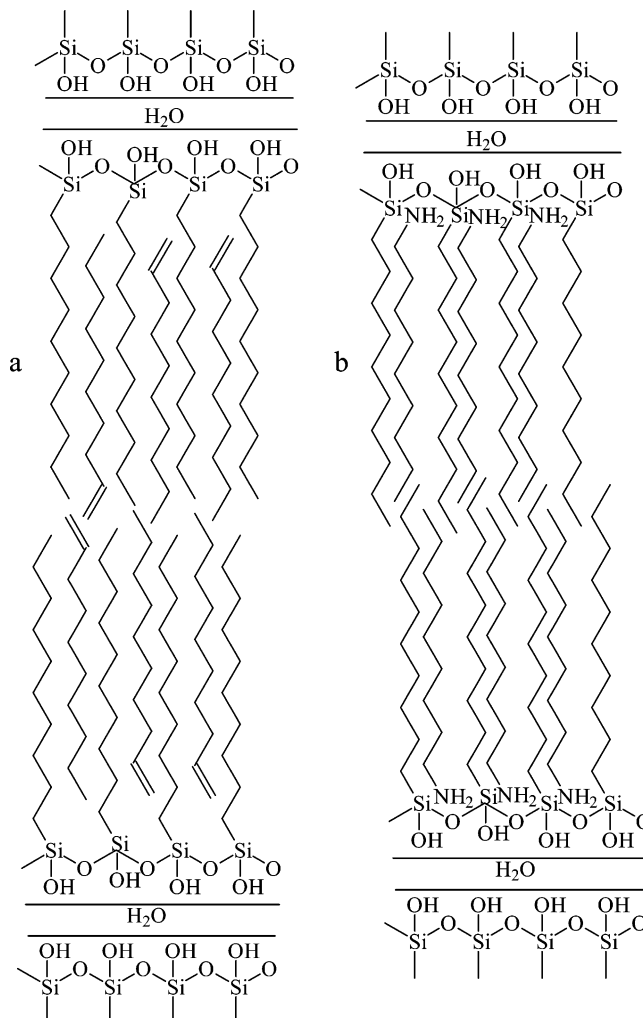


Figure 2. Electron density profiles along the lamellar normal in the pristine and functionality-enhanced PODS generated by one-dimensional Fourier transformation of the corresponding SAXS data in Figure 1.

acid is added to PODS/ODA, protonation of the amino groups occurs, as depicted in Scheme 2, and the resulting divalent  $\text{PtCl}_6^{2-}$  anion subsequently interacts with two ODA molecules. As discussed above, ODA molecules may hydrogen-bond to silanol groups in the siloxy bilayer, in which case interaction with  $\text{PtCl}_6^{2-}$  ions could bring the complexes in close proximity to, if not inside, the siloxy bilayer. This arrangement explains the increase in the apparent siloxy bilayer size. Concurrently, the pair of protonated ODA molecules interacting with each  $\text{PtCl}_6^{2-}$  ion should distort the hydrocarbon tail layer (see Scheme 2).

Reduction of the Pt complex with  $\text{NaBH}_4$  effectively restores the PODS/ODA nanostructure. The half-width of the central peak returns to  $\sim 1$  nm, and the compressed tail region expands back to the level of pristine PODS. After reduction with  $\text{H}_2$ , however, the structural distortion of the PODS/ODA matrix is partially preserved. The central peak corresponding to the siloxy bilayer remains enlarged at a half-width of 1.2 nm, and the electron density of the alkyl tails continues to be relatively high. The marked difference in the structure of the siloxy bilayer of the two Pt-filled PODS/ODA samples can be attributed to the efficacy of the reducing agents to penetrate the siloxy bilayer and promote nanoparticle formation. Gaseous  $\text{H}_2$  readily diffuses through the hydrophobic layers and nucleates nanoparticle formation in the siloxy bilayer, which is consequently broadened. Nucleation and growth of Pt nanoparticles outside the siloxy bilayer (within the hydrophobic tails) will presumably

SCHEME 1. Schematic Diagrams of (a) the PODS/ODC and (b) the PODS/ODA Systems (for the sake of illustration, alkyl chains are not drawn to scale)



serve to disorder the lamellar nanostructure and, thus, decrease the local electron density. Incorporation of  $\text{NaBH}_4$  inside the PODS/ODA- $\text{H}_2\text{PtCl}_6$  system may be impeded by the hydrophobic alkyl tails, in which case complex reduction and nanoparticle nucleation more probably commence outside the siloxy bilayer. In this event, Pt ions are prone to migrate out of (thereby reducing the width of) the siloxy bilayer to join growing Pt nanoparticles. For both reducing agents, the distorted  $\text{PtCl}_6^{2-}$ -(ODA $\text{H}^+$ )<sub>2</sub> complex disappears altogether after reduction, and so no significant deformation is observed in the density profiles of the hydrocarbon tails.

**Morphology of Modified Pt-Filled PODS.** The location and morphology of Pt nanoparticles generated in Pt-filled PODS/FM systems have been directly visualized by TEM. Representative TEM images of PODS/ODC systems filled with Pt

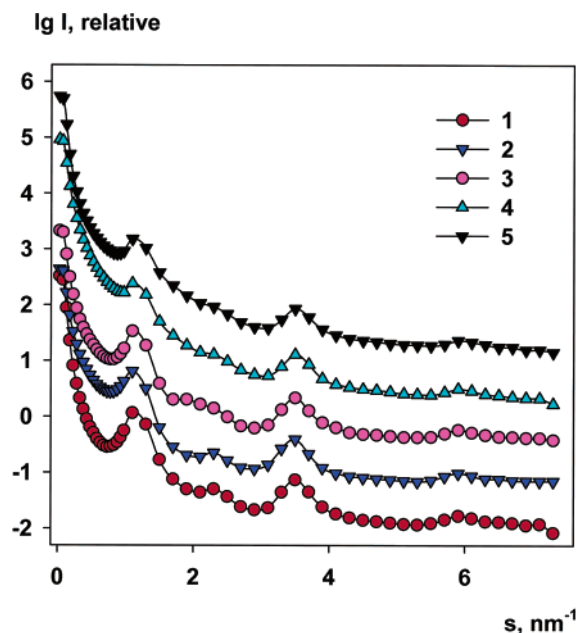


**Figure 3.** SAXS patterns collected from the PODS/ODC system far from the absorption edge. The datasets correspond to PODS (1), PODS/ODC (2), PODS/ODC-K[PtCl<sub>3</sub>] $\cdot$ H<sub>2</sub>O (3), and PODS/ODC-K[PtCl<sub>3</sub>] $\cdot$ H<sub>2</sub>O after reduction with NaBH<sub>4</sub> (4) and H<sub>2</sub> (5).

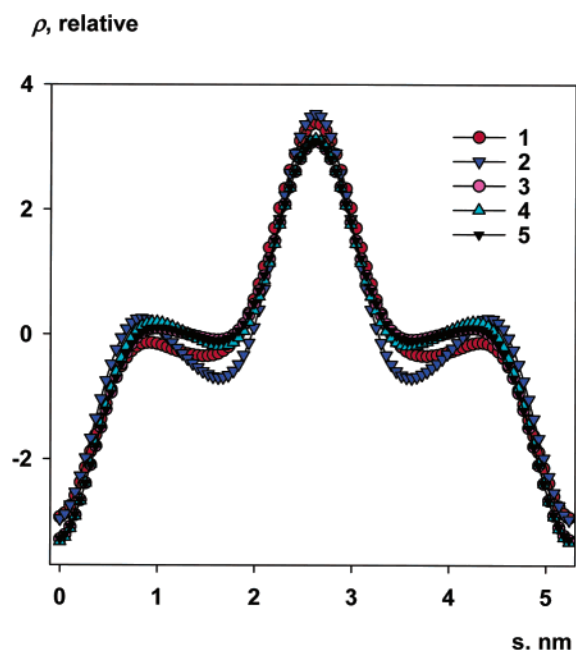


**Figure 4.** Electron density profiles along the lamellar normal in the PODS/ODC system generated by one-dimensional Fourier transformation of the corresponding SAXS data in Figure 3.

nanoparticles after NaBH<sub>4</sub> and H<sub>2</sub> reduction of the precursor material (with Zeise salt) are displayed in Figures 7a, b and c, respectively. Reduction of the salt complex with NaBH<sub>4</sub> results in the formation of two populations of nanoparticles: (i) a significant number of large, randomly located and irregularly shaped particles, and (ii) small nanoparticles measuring about 1 nm in diameter, regularly positioned in the lamellar matrix (cf. Figure 7b). In marked contrast, H<sub>2</sub> reduction results in a more uniform material with prevailing 1 nm nanoparticles located along the siloxy bilayers. Very few large, irregular particles are evident in this system. These observations can be explained on the basis of the PODS/ODC system during reduction. The double bonds of ODC undergo complexation

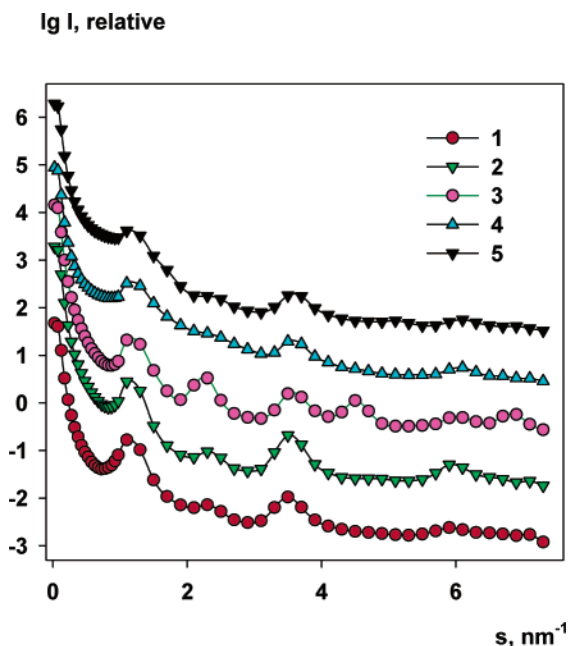


**Figure 5.** SAXS patterns collected from the PODS/ODA system far from the absorption edge. The datasets correspond to PODS (1), PODS/ODA (2), PODS/ODA-H<sub>2</sub>PtCl<sub>6</sub> (3), and PODS/ODA-H<sub>2</sub>PtCl<sub>6</sub> after reduction with NaBH<sub>4</sub> (4) and H<sub>2</sub> (5).

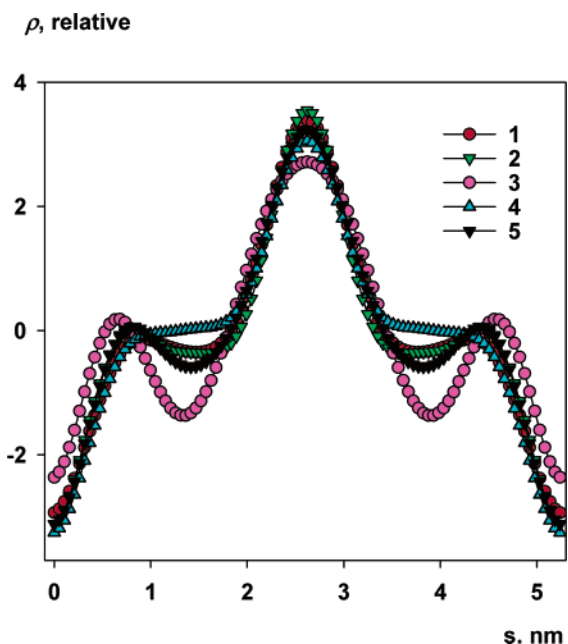
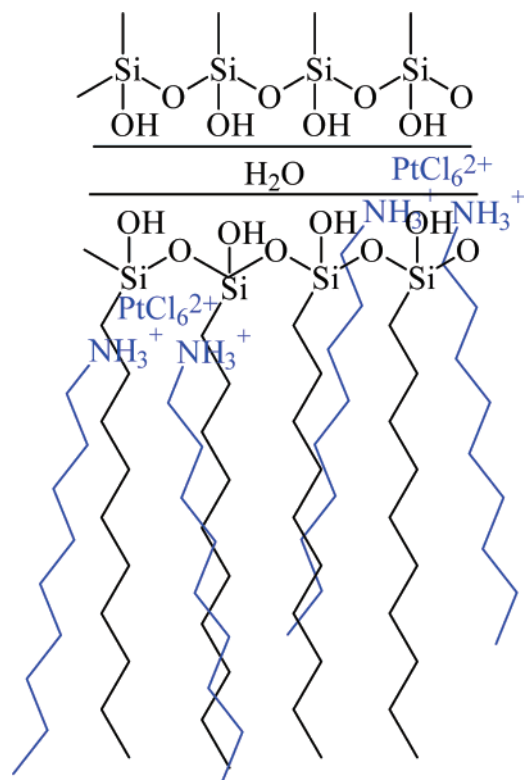


**Figure 6.** Electron density profiles along the lamellar normal in the PODS/ODA system generated by one-dimensional Fourier transformation of the corresponding SAXS data in Figure 5.

with the Zeise salt, but do not specifically adsorb on the growing nanoparticle surface, although hydrophobic environments are known to control nanoparticle growth.<sup>43,44</sup> Thus, if nanoparticle formation occurs in the well-ordered vicinity of the siloxy bilayer, small nanoparticles can be stabilized. If, on the other hand, nucleation proceeds in the less ordered alkyl layer, particle growth is anticipated to be almost completely unrestricted, resulting in the formation of uncontrollably large particles (cf. Figure 7a). The difference between the two reducing agents can be attributed to the nucleation rate. Normally NaBH<sub>4</sub> is a fast-working reducing agent that typically yields relatively small nanoparticles. Since, however, PODS/ODC is a very hydrophobic material, penetration of polar NaBH<sub>4</sub> inside the hydro-



**SCHEME 2. Schematic Depiction of the Distortion in the PODS/ODA Structure after Introduction of  $\text{H}_2\text{PtCl}_6 \cdot 6\text{H}_2\text{O}$**



phobic layer is most likely hindered, resulting in slow and irregular reduction and subsequent particle nucleation. On the contrary, gaseous  $\text{H}_2$  penetration is not at all obstructed, thereby ensuring rapid reduction of the Zeise salt and nucleation of relatively monodisperse Pt nanoparticles (cf. Figure 7c).

Similar events occurring in the PODS/ODA system produce very different materials. According to TEM images, such as the ones presented in Figure 8a,b,  $\text{NaBH}_4$  reduction results in the formation of two populations of nanoparticles measuring  $\sim 1$  and  $\sim 2$  nm in diameter. Smaller particles appear to be located along (or inside) the siloxy bilayers, while the marginally larger particles are not coordinated with respect to the lamellar matrix. In contrast,  $\text{H}_2$  reduction yields only small nanoparticles with a mean diameter of  $\sim 1$  nm (cf. Figures 8c,d). Their position appears to be highly commensurate with the lamellar nanostructure. While the considerations discussed above regarding reduction in the PODS/ODC system remain applicable here, two additional factors affecting reduction in the PODS/ODA system must also be considered: (i) penetration of  $\text{NaBH}_4$  may be faster in PODS/ODA than in PODS/ODC since the PODS/ODA matrix contains more polar (amino) groups that can serve to facilitate molecular transport, and (ii) ODA is expected to specifically adsorb on the nanoparticle surface, thereby stabilizing nanoparticle growth.<sup>14</sup> In light of these differences, it is not surprising that  $\text{H}_2$  reduction yields remarkably uniform 1 nm nanoparticles regularly spaced within the lamellar matrix of the PODS/ODA system. It should also be noted that the degree of lamellar ordering evident in the reduced PODS/ODC and PODS/ODA systems featured in Figures 7 and 8, respectively, is the highest for (both) systems subjected to  $\text{H}_2$  reduction, which is consistent with its anticipated efficiency in both hydrophobic (ODC-rich) and hydrophilic (ODA-rich) polymer matrices.

**Size Characteristics of Modified Pt-Filled PODS.** To isolate the scattering signal from Pt nanoparticles, we have calculated

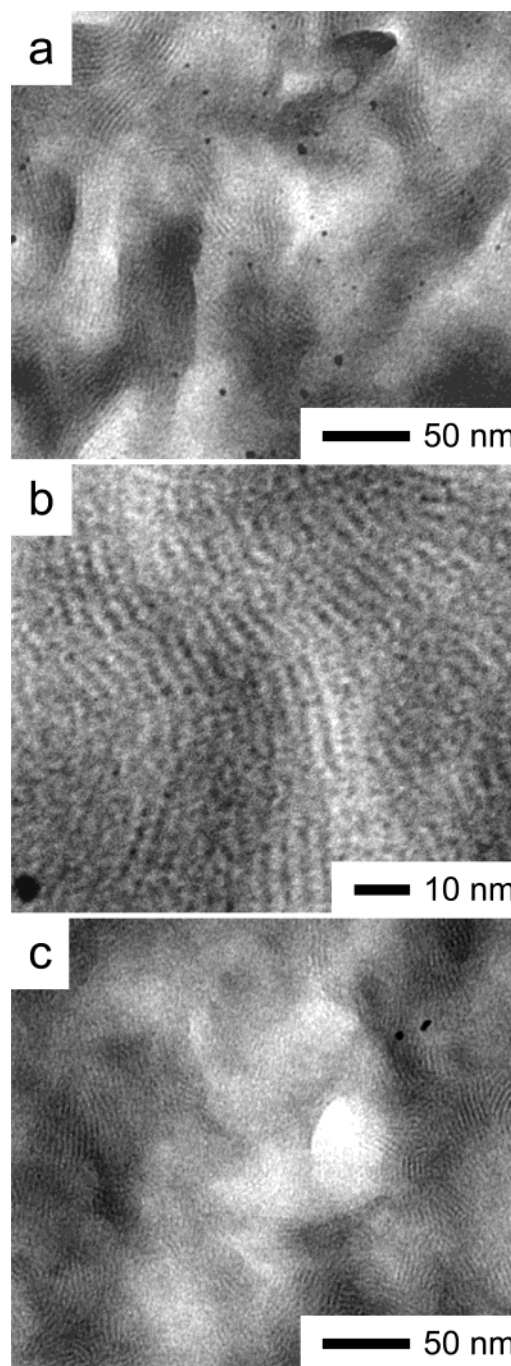


**Figure 7.** TEM images of the PODS/ODC- $\text{K}[\text{PtCl}_3] \cdot \text{H}_2\text{O}$  system with Pt nanoparticles obtained after reduction with (a,b)  $\text{NaBH}_4$  and (c)  $\text{H}_2$ . The siloxy bilayer of PODS and the Pt nanoparticles appear electron-opaque (dark) in these images.

differences between SAXS intensities at several incident-beam energies. In principle, the Bragg peaks corresponding to the lamellar nanostructure of the PODS matrix should disappear completely in such difference curves. Figure 9 attests, however, that these peaks remain partially preserved. A plausible explanation for this unexpected observation will be proposed after examination of the size distribution functions computed for the Pt nanoparticles. With this limitation notwithstanding, however, the intensity differences obtained in this fashion are proportional to the expected anomalous signal from the Pt atoms. Size distribution functions of metal-containing samples generated from such difference curves are displayed for comparison in Figures 10 and 11 for the PODS/ODC and PODS/ODA systems, respectively. The distributions of Pt species in the PODS/ODC

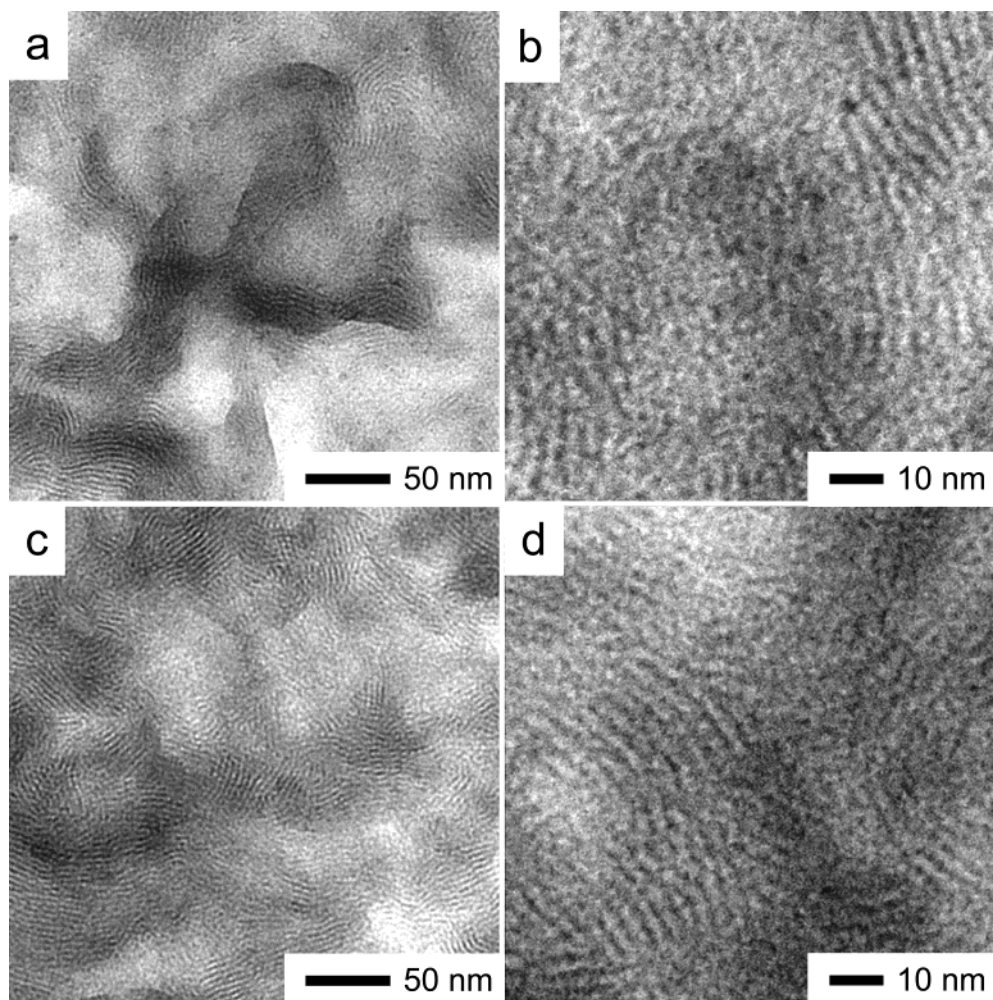


**Figure 8.** TEM images of the PODS/ODA–H<sub>2</sub>PtCl<sub>6</sub> system with Pt nanoparticles obtained after reduction with (a,b) NaBH<sub>4</sub> and (c,d) H<sub>2</sub>. The siloxy bilayer of PODS and the Pt nanoparticles appear electron-opaque (dark) in these images.

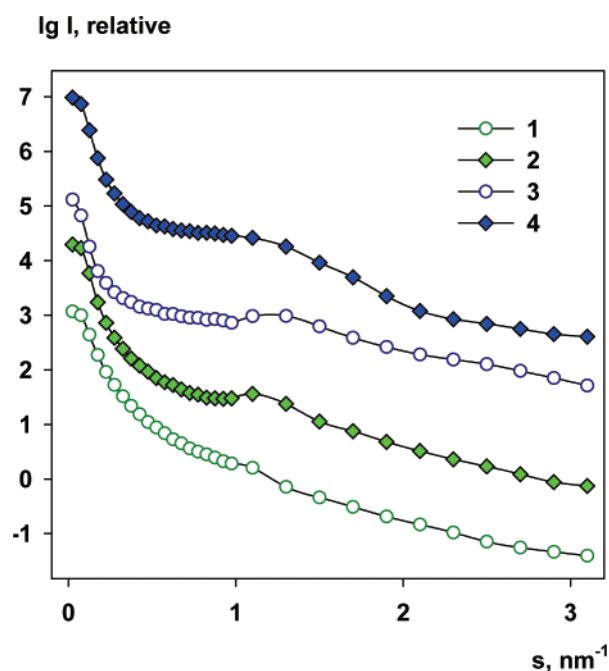


**Figure 9.** Difference ASAXS data (anomalous signal) from the Pt-containing PODS/ODC (1, 2) and PODS/ODA (3, 4) after reduction with NaBH<sub>4</sub> (1, 3) and H<sub>2</sub> (2, 4).

system (Figure 10) demonstrate the existence of a large population of small nanoparticles with radii measuring 2.0–

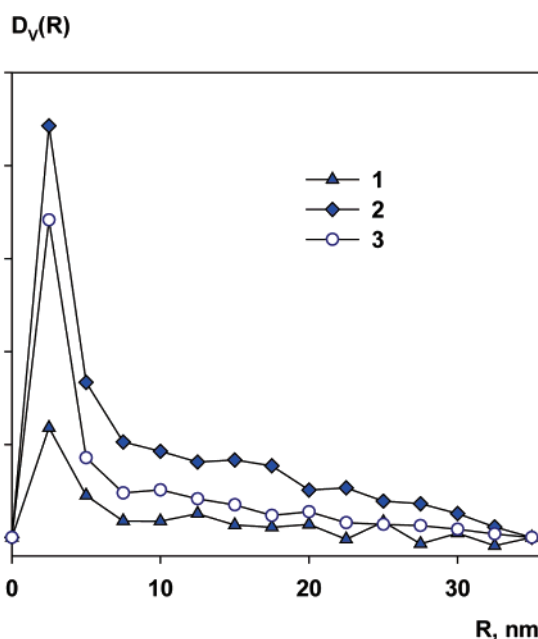


**Figure 10.** Size distribution functions of the Pt species in the PODS/ODC–K[PtCl<sub>3</sub>]·H<sub>2</sub>O system before (1) and after reduction with NaBH<sub>4</sub> (2) and H<sub>2</sub> (3).

2.5 nm. Note that these distributions closely resemble that of Pt salt clusters in the nanoparticle precursors. Figure 10 also reveals the presence of a broad fraction of larger particles (with



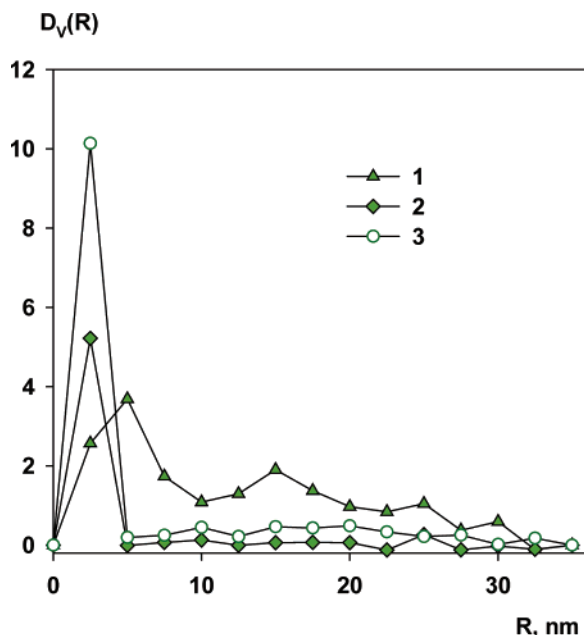
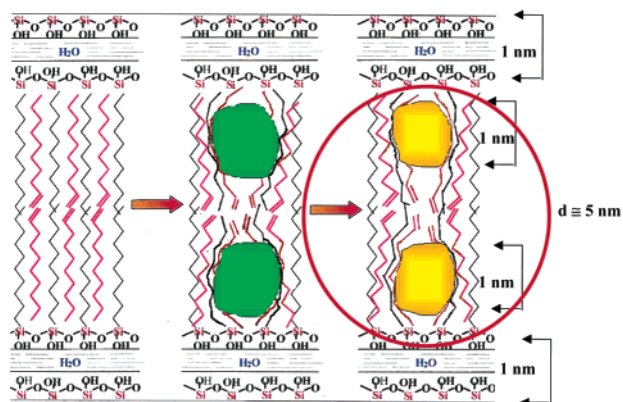


**Figure 11.** Size distribution functions of the Pt species in the PODS/ODA- $\text{H}_2\text{PtCl}_6$  system before (1) and after reduction with  $\text{NaBH}_4$  (2) and  $\text{H}_2$  (3).

**SCHEME 3. Schematic Illustration of PODS after Intercalation of a Functional Modifier (maroon), a Pt Compound (green) and the Formation of a Pt Metal Nanoparticle (yellow)**



radii up to 35 nm). These large particles are obtained after reduction with either  $\text{NaBH}_4$  or  $\text{H}_2$ , but appear to be systematically larger and more abundant after  $\text{NaBH}_4$  reduction. This size distribution trend is not, however, observed in the PODS/ODA functionalized medium. In the case of the PODS/ODA system (Figure 11), salt clusters possess a very broad size distribution, with the principal maximum centered at  $\sim 5$  nm. After reduction with either  $\text{NaBH}_4$  or  $\text{H}_2$ , however, the Pt size distributions show that the resultant nanoparticles are, for the most part, smaller. The diameter of the scattering nanoparticles obtained using both reducing agents is about 5 nm, which closely matches the lamellar period in PODS but differs from the Pt nanoparticle sizes discerned by TEM. This discrepancy, along with the preservation of Bragg peaks (from the lamellar PODS nanostructure) in the difference curves (Figure 9) used to compute the particle size distributions (Figures 10 and 11), must be explained.

The disparate TEM and SAXS results can be reconciled by the conceptual model depicted in Scheme 3, wherein nanoparticle aggregates produced inside the alkyl tail regions constitute the primary nanoparticles detected by ASAXS. Due

to the dense packing of individual Pt nanoparticles measuring  $\sim 1$  nm in diameter (evidenced by TEM), SAXS identifies nanoparticle ensembles formed in FM-rich locations, which are distributed irregularly throughout the PODS bilayers. Recall from the elemental analysis in Table 1 that the PODS/ODC system contains one ODC molecule for each four PODS units, and that the FM molecules most likely segregate. It immediately follows that the  $\text{K}[(\text{ODC})\text{PtCl}_3]$  molecules would assemble into clusters after addition of the Zeise salt, while other areas would remain free of Pt compounds. Incorporated polar species are expected to collect along both sides of the siloxy layers, thereby forming two parallel rows of Pt-containing conglomerations according to the location of the charged group (see Scheme 1). In ASAXS, these binary metalated regions will scatter as Pt compound clusters possessing diameters of about 5 nm (the lamellar  $d$  spacing) and will contribute to the same Bragg peaks as the organized motif of the PODS nanostructure. When Pt nanoparticles are formed upon chemical reduction, they remain positioned along the siloxy bilayer since they nucleate from the Pt precursor. This process not only preserves the primary nanoparticle size but also permits the formation of large, irregular nanoparticles that are randomly located due to the low concentration of ODC in the system. These large particles, evident in Figure 7a, are presumed to form in FM-rich regions that are incommensurate with the lamellar pattern. Figure 7b also displays double rows of small Pt nanoparticles, regularly located along the electron-dense (dark) siloxy bilayers, which further supports this proposed model.

Now let us consider the more chemically complex PODS/ODA system, which, according to the elemental data listed in Table 1, contains double the amount of FM. On this basis, coupled with the possibility that the amine group on ODA locates near the polar siloxy bilayer and the water channel intercalated therein, the PODS/ODA system is expected to produce a more uniform material. Nevertheless, the same reasoning provided above remains applicable with one notable exception: the PODS/ODA system contains platonic acid. The mean cluster diameter of platonic acid is about 10 nm, which is about twice the  $d$  spacing of the functionalized polymer matrix. As discussed above, the Pt precursor penetrates the siloxy bilayer and the bilayer size changes accordingly, in which case the size of the scattering elements may increase beyond the lamellar period. After reduction, however, the scattering size returns to match the lamellar size. Thus, we conclude that, due to the complex aggregation phenomena expected and observed in these functionalized systems, ASAXS is unable to yield information on the size distribution of individual Pt nanoparticles. Instead, it provides information regarding the clustering of nanoparticles before and after reduction.

## Conclusions

To enhance the functionality of PODS, an amphiphilic polymer that self-organizes into a lamellar matrix, for use as a nanoparticle growth medium, we have prepared hybrid materials by intercalating two functional modifiers (ODC and ODA) into the otherwise unused hydrophobic regions of PODS. Anomalous and conventional SAXS, as well as TEM, have been used to explore the morphology and location of Pt nanoparticles produced in these functionality-enhanced bicomponent materials. When Pt compounds are incorporated into these hybrid systems and Pt species are subsequently reduced with either  $\text{NaBH}_4$  or  $\text{H}_2$ , the nanostructure of the polymer matrix transforms to different extents. Relatively minor changes are observed for the system derived from PODS/ODC and  $\text{K}[(\text{C}_2\text{H}_4)\text{PtCl}_3] \cdot \text{H}_2\text{O}$ ,

which implies that the Pt complexes and their reduced nanoparticles in this case localize along the siloxy bilayers, but not inside them. Electron density profiles computed for the PODS/ODA system after interaction with  $\text{H}_2\text{PtCl}_6 \cdot 6\text{H}_2\text{O}$  suggest that  $\text{PtCl}_6^{2-}$  ions are partially incorporated into, and thus broaden, the siloxy bilayer. Simultaneous distortion of the hydrophobic layer occurs due to the concurrent formation of  $(\text{PtCl}_6^{2-})-(\text{ODAH}^+)_2$  molecules. Further reduction with  $\text{NaBH}_4$  effectively restores the inherent PODS nanostructure, while  $\text{H}_2$  reduction retains a partially distorted lamellar morphology, which might be caused by the limited presence of Pt nanoparticles inside the siloxy bilayer. Examination of these hybrid materials by TEM confirms that all the samples contain small ( $\sim 1$  nm diameter) Pt nanoparticles, which tend to localize in commensurate fashion with the pattern of the lamellar matrix. In addition to such nanoparticles, the PODS/ODA system contains much larger, irregularly shaped, and irregularly located nanoparticles whose fraction depends on the type of reducing agent. Conversely, the PODS/ODA system contains either a single population of small ( $\sim 1$  nm) nanoparticles with  $\text{H}_2$  reduction or two populations of nanoparticles ( $\sim 1$  and  $2$  nm) with  $\text{NaBH}_4$  reduction.

The difference between the two systems can be attributed to (i) the higher concentration of ODA molecules in PODS and (ii) specific adsorption of ODA amino groups on the nanoparticle surface. Furthermore, the difference between the two reducing agents,  $\text{NaBH}_4$  and  $\text{H}_2$ , is explained on the basis of their ability to penetrate through the hydrophobic layers and nucleate nanoparticle growth. Since these functionality-enhanced hybrid materials (in particular, the PODS/ODA system) are, for the most part, hydrophobic, penetration of polar  $\text{NaBH}_4$  inside the hydrophobic layer appears to be hindered, resulting in slow and irregular nanoparticle nucleation. In marked contrast, gaseous  $\text{H}_2$  penetration is not obstructed, thus leading to fast and relatively uniform nucleation. Size distribution functions computed from SAXS for Pt species in the hybrid materials filled with nanoparticles demonstrate that the majority of the scattering elements measure  $\sim 5$  nm in diameter. This result suggests that the  $\sim 1$  nm nanoparticles imaged by TEM decorate the siloxy bilayer and aggregate into nanoparticle clusters formed by segregated FMs, whereas regions between these clusters are presumed to be free from Pt species, which further confirms the prominent location of nanoparticles along the siloxy bilayer. We contend that highly functional and ordered systems such as hybrid PODS/ODA can be used for the controlled formation and positioning of different types of nanoparticles (e.g., magnetic or quantum dots), thereby allowing enhancement of the material properties. In addition to providing fundamental insight into the functionalization of PODS through the intercalation of ODC or ODA for controlled nanoparticle growth, this study also underlines the tremendous benefit of combined (A)SAXS and TEM analyses and demonstrates how the two analytical methods synergistically yield a clear representation of the structure of inorganic nanoscale objects within organic nanostructured matrices.

**Acknowledgment.** The authors acknowledge the financial support provided by the Presidium of the Russian Academy of Science, Grant No 03-27 "Fundamental problems of physics and chemistry of nanosized systems and nanomaterials," the Russian Foundation for Basic Research (Grant Nos. 01-03-32937 and 02-03-32613), NATO Science for Peace Program (grant SfP-974173), and the INTAS (International Association for the Promotion of Cooperation with Scientists from New

Independent States of the former Soviet Union, Grant No. 00-243). R.J.S. gratefully thanks the Alexander von Humboldt Foundation for funding, and the Institut für Makromolekulare Chemie at the Albert-Ludwigs Universität Freiburg for the generous provision of facilities.

## References and Notes

- (1) Chan, Y. N. C.; Schrock, R. R.; Cohen, R. E. *J. Am. Chem. Soc.* **1992**, *114*, 7295.
- (2) Ciebiën, J. F.; Clay, R. T.; Sohn, B. H.; Cohen, R. *New J. Chem.* **1998**, *22*, 685.
- (3) Cummins, C. C.; Schrock, R. R.; Cohen, R. E. *Chem. Mater.* **1992**, *4*, 27.
- (4) Moffitt, M.; McMahon, L.; Pessel, V.; Eisenberg, A. *Chem. Mater.* **1995**, *7*, 1185.
- (5) Moffitt, M.; Vali, H.; Eisenberg, A. *Chem. Mater.* **1998**, *10*, 1021.
- (6) Antonietti, M.; Wenz, E.; Bronstein, L.; Seregina, M. *Adv. Mater.* **1995**, *7*, 1000.
- (7) Spatz, J. P.; Roescher, A.; Möller, M. *Adv. Mater.* **1996**, *8*, 337.
- (8) Hashimoto, T.; Harada, M.; Sakamoto, N. *Macromolecules* **1999**, *32*, 6867.
- (9) Underhill, R. S.; Liu, G. *Chem. Mater.* **2000**, *12*, 2082.
- (10) Zhao, M.; Crooks, R. M. *Adv. Mater.* **1999**, *11*, 217.
- (11) Mayer, A. B. R.; Mark, J. E. *Colloid Polym. Sci.* **1997**, *275*, 333.
- (12) Lu, Z.; Liu, G.; Phillips, H.; Hill, J. M.; Chang, J.; Kydd, R. A. *Nano Lett.* **2001**, *1*, 683.
- (13) Sidorov, S. N.; Bronstein, L. M.; Davankov, V. A.; Tsyurupa, M. P.; Solodovnikov, S. P.; Valetsky, P. M.; Wilder, E. A.; Spontak, R. J. *Chem. Mater.* **1999**, *11*, 3210.
- (14) Sidorov, S. N.; Bronstein, L. M.; Valetsky, P. M.; Hartmann, J.; Colfen, H.; Schnablegger, H.; Antonietti, M. *J. Colloid Interface Sci.* **1999**, *212*, 197.
- (15) Kotov, N. A.; Dekany, I.; Fendler, J. H. *J. Phys. Chem.* **1995**, *99*, 13065.
- (16) Bronstein, L. M.; Chernyshov, D. M.; Valetsky, P. M.; Wilder, E. A.; Spontak, R. J. *Langmuir* **2000**, *16*, 8221.
- (17) Svergun, D. I.; Kozin, M. B.; Konarev, P. V.; Shtykova, E. V.; Volkov, V. V.; Chernyshov, D. M.; Valetsky, P. M.; Bronstein, L. M. *Chem. Mater.* **2000**, *12*, 3552.
- (18) Spatz, J. P.; Herzog, T.; Mössmer, S.; Ziemann, P.; Möller, M. *Adv. Mater.* **1999**, *11*, 149.
- (19) Seregina, M. V.; Bronstein, L. M.; Platonova, O. A.; Chernyshov, D. M.; Valetsky, P. M.; Hartmann, J.; Wenz, E.; Antonietti, M. *Chem. Mater.* **1997**, *9*, 923.
- (20) Esumi, K.; Suzuki, A.; Aihara, N.; Usui, K.; Torigoe, K. *Langmuir* **1998**, *14*, 3157.
- (21) Gröhn, F.; Bauer, B. J.; Akpalu, Y. A.; Jackson, C. L.; Amis, E. J. *Macromolecules* **2000**, *33*, 6042.
- (22) Thurmond, K. B., II; Kowalewski, T.; Wooley, K. L. *J. Am. Chem. Soc.* **1996**, *118*, 7239.
- (23) Bronstein, L. M.; Linton, C.; Karlinsey, R.; Stein, B.; Svergun, D. I.; Zwanziger, J. W.; Spontak, R. J. *Nano Lett.* **2002**, *2*, 873.
- (24) Bronstein, L. M.; Linton, C. N.; Karlinsey, R.; Ashcraft, E.; Stein, B. D.; Svergun, D. I.; Kozin, M.; Khotina, I. A.; Spontak, R. J.; Werner-Zwanziger, U.; Zwanziger, J. W. *Langmuir* **2003**, *19*, 7071.
- (25) Sankaran, V.; Cummins, C. C.; Schrock, R. R.; Cohen, R. E.; Silbey, R. J. *J. Am. Chem. Soc.* **1990**, *112*, 6858.
- (26) Sohn, B. H.; Kim, T. H.; Char, K. *Langmuir* **2002**, *18*, 7770.
- (27) Bochenkov, V. E.; Stephan, N.; Brehmer, L.; Zagorskii, V. V.; Sergeev, G. B. *Colloids Surf. A* **2002**, *198–200*, 911.
- (28) Bronstein, L. M.; Chernyshov, D. M.; Volkov, I. O.; Ezernitskaya, M. G.; Valetsky, P. M.; Matveeva, V. G.; Sulman, E. M. *J. Catal.* **2000**, *196*, 302.
- (29) Rutnakornpituk, M.; Thompson, M. S.; Harris, L. A.; Farmer, K. E.; Esker, A. R.; Riffle, J. S.; Connolly, J.; St. Pierre, T. G. *Polymer* **2002**, *43*, 2337.
- (30) Bronstein, L.; Seregina, M.; Valetsky, P.; Breiner, U.; Abetz, V.; Stadler, R. *Polym. Bull.* **1997**, *39*, 361.
- (31) Parikh, A. N.; Schivley, M. A.; Koo, E.; Seshadri, K.; Aurentz, D.; Mueller, K.; Allara, D. L. *J. Am. Chem. Soc.* **1997**, *119*, 3135.
- (32) Stuhmann, H. B.; Goerigk, G.; Munk, B. In *Handbook on Synchrotron Radiation*; Koch, M., Ed.; Elsevier: Amsterdam, 1994; p 555.
- (33) Haubold, H.-G.; Wang, X. H.; Goerigk, G.; Schilling, W. *J. Appl. Crystallogr.* **1997**, *30*, 653.
- (34) Svergun, D. I.; Shtykova, E. V.; Kozin, M. B.; Volkov, V. V.; Dembo, A. T.; Shtykova, E. V. J.; Bronstein, L. M.; Platonova, O. A.; Yakunin, A. N.; Valetsky, P. M.; Khokhlov, A. R. *J. Phys. Chem. B* **2000**, *104*, 5242.
- (35) Haubold, H.-G.; Gebhardt, R.; Buth, G.; Goerigk, G. In *Resonant Anomalous X-ray Scattering*; Fischer, K., Ed.; Elsevier: Oxford, 1994; pp 295.

- (36) Haubold, H.-G. *J. Phys. IV. C8, (Suppl. J. Phys. I)* **1993**, 3, 475.
- (37) Haubold, H.-G.; Gruenhagen, K.; Wagener, M.; Jungbluth, H.; Heer, H.; Pfeil, A.; Rongen, H.; Brandenburg, G.; Moeller, R.; Matzerath, J.; Hiller, P.; Halling, H. *Rev. Sci. Instrum.* **1989**, 60, 1943.
- (38) Svergun, D. I. *J. Appl. Crystallogr.* **1992**, 25, 495.
- (39) Konarev, P. V.; Volkov, V. V.; Sokolova, A. V.; Koch, M. H. J.; Svergun, D. I. *J. Appl. Crystallogr.* **2003**, 36, 1277.
- (40) Vainshtein, B. K. *Diffraction of X-rays by Chain Molecules*; Elsevier: Amsterdam, 1966.
- (41) Fritz, H. P.; Schwarzhans, K. E.; Sellmann, D. *J. Organomet. Chem.* **1966**, 6, 551.
- (42) Abel, E. W. *Comprehensive Organometallic Chemistry: The Synthesis, Reactions, and Structures of Organometallic Compounds*; Pergamon Press: Oxford, 1982.
- (43) Eiser, E.; Bouchama, F.; Thathagar, M. B.; Rothenberg, G. *ChemPhysChem* **2003**, 4, 526.
- (44) Yonezawa, T.; Toshima, N.; Wakai, C.; Nakahara, M.; Nishinaka, M.; Tominaga, T.; Nomura, H. *Colloids Surf. A* **2000**, 169, 35.